Engineering characterization of the novel Bach impeller for bioprocessing applications requiring low power inputs

Tom A. Wyrobnik[ab], Steve Oh[b], Andrea Ducci[c], Martina Micheletti[a*]

[a] Department of Biochemical Engineering, UCL, Gower Street, London WC1E 6BT, UK

[b] Bioprocessing Technology Institute, A*STAR, 20 Biopolis Way, Singapore, Singapore

[c] Department of Mechanical Engineering, UCL, Torrington Place, London WC1E 7JE, UK

*Correspondence to: Martina Micheletti

Email: m.micheletti@ucl.ac.uk

Abstract

The choice of impeller design in stirred-tank reactors (STRs) affects important process characteristics such as the suspension of particulates, mixing of nutrients or gasses, and the distribution of turbulent kinetic energy and its dissipation rate. A novel impeller, the Bach impeller, has been characterized in this work and its novel geometry and mechanism of action are discussed in detail. Experimental measurements of the power consumption, mixing time, and microparticles suspension dynamics were carried out at the 1 L scale in an unbaffled reactor and the performance compared with two conventional up-pumping axial flow impellers, namely the 3-Blade segment (3BS, also called "elephant ear") and marine impeller. In addition, the impeller flow number and pumping efficiency were obtained from Particle Image Velocimetry experiments. The Bach impeller exhibited a low power number of N_P=0.36 and showed it can generate a uniform suspension of microcarriers even at relatively low impeller speeds (from N=25-30 rpm onwards). The impeller was found to effectively mix the reactor volume within t_M=25 s at N>50 rpm (i.e. Nt_M=37±5) at a higher clearance when it was mounted closer to the free surface, C/T>0.5, while minimally affecting its suspension capabilities. Lastly, the Bach impeller displaced more fluid than the marine impeller and roughly an equal amount to the 3BS impeller, suggesting that the novel impeller can successfully be used for STR processes in the (bio)chemical engineering industry where low power inputs, but high mixing and particle suspension efficiencies are sought.

1. Introduction

Stirred-tank reactors (STRs) are widely used as a scalable production platform for a large variety of products related to the chemical engineering, pharmaceutical production, food processing, or bioprocess engineering industries. Within the bioprocessing industry, the use of STRs has enabled the manufacture of large quantities of monoclonal antibodies, vaccines, and other recombinant protein therapeutics. More recently, stem cells have been expanded in STRs to produce cell and gene therapies or cultivated meat products (Hanga et al., 2020; Odeleye et al., 2013; Rafiq et al., 2013). When expanding biological organisms in STRs, optimizing the growth environment via adjustments in hydrodynamics is an important aspect of process development efforts. The bioreactor hydrodynamics generated by impellers or other types of rotating motion are known to affect cell cultures which will respond with changes in metabolism, proliferation, or differentiation (Chalmers, 2015; Weyand et al., 2009). Studies on the lethality of shear stress exposure reported limits to be in the range of 1-10 Pa for antibody producing suspension cell lines (Cherry, 1993; Chisti, 2001). Pluripotent stem cells have been found to be less tolerant, with their differentiation being promoted by shear stresses in the range of 0.15 Pa − 1 Pa (Yamamoto et al., 2005) and 1.5 Pa (Ahsan and Nerem, 2010). Studying the characteristic flow environment of a bioreactor system is also critical from a scaling-up perspective, where key engineering parameters must be identified to be used as scaling criteria and act as boundaries of a design space in which the bioprocess can be performed at larger scales.

In the stirred tank, the impeller is the major factor responsible for mixing efficiency, quality of microcarriers' suspension, dissipation of turbulent kinetic energy, and both macro and micro fluid flow scales. As such, it is a crucial design aspect of reactors which directly influences the success of biopharmaceutical production batches. It is obvious that depending on the cell type and target product, some impellers may be more suitable than others. Indeed, the large variety of cell types and applications for which stirred-tank bioreactors have been used necessitated the development of a multitude of stirrer designs to meet the specific needs of the production system and mitigate risks depending on the processing requirements of the biological entities (Böhm et al., 2019). A common goal of impeller design and development, however, may be formulated as achieving efficient mixing, off-bottom suspension, and solids homogenization (if required) at the lowest possible power input (Jaszczur et al., 2020).

Frequently used impellers for low power input applications include variations of the 3-Blade Segment (3BS) impeller (e.g., from Sartorius AG, Germany) or the marine impeller (e.g., from Merck KGaA, Germany) (Wyrobnik et al., 2020). These standard impellers have been modified to reduce shear stress levels (Jossen et al., 2014), or power input (Loubière et al., 2019; Rotondi et al., 2021). Bliatsiou et al. (Bliatsiou et al., 2019) developed multiple variations of Rushton and pitched blade turbines with the goal of identifying geometrical modifications that would reduce particle breakage for shear stress sensitive applications. However, even though small impeller modifications of existing designs showed significant improvement of flow characteristics and impeller performance, impellers have not often been developed *de novo* and only few attempts of designing novel impellers that specifically address the challenges found in cell manufacturing are reported in the literature. One such example is the development of the vertical Ferris wheel impeller, patented by PBS Biotech, though its design does not fit into traditional stirred tanks and thus requires different infrastructure (de Sousa Pinto et al., 2019). In addition, it is also worth noting that alternative mixing innovations that do not rely on impeller agitation were proposed for the bioprocess industry, including amongst others orbitally shaken bioreactors (Klöckner et al., 2014) or WAVE bioreactors (Singh, 1999).

In this study, we present a rigorous experimental engineering characterization for a newly developed impeller, called Bach impeller (Cellmotions Inc., Canada). The Bach impeller has an unconventional design with a central spiral that is surrounded by five vanes/blades (Figure 1, A). Through the rotating spiral, the impeller induces a different type of fluid motion in comparison to conventional axial flow impellers that rely on the blades to generate bulk fluid motion. The fluid follows an upwards axial vortex before being forced tangentially trough the vanes and as such is expected to support solids suspension. In addition, the Bach impeller blades have been designed to reduce drag in clockwise rotation and are therefore theorized to have less impact on biological entities than flat blade impellers. The main objective of this work is to introduce the novel design and to show its potential suitability for use in low power input bioprocessing applications. We identify in detail how its features affect mixing and flow characteristics in a 1 L stirred tank reactor. As such, we anticipate this work to facilitate adoption of this impeller for chemical and bioprocess engineers who are interested in exploring alternative agitation solutions in stirred tanks. The results provided in this work will furthermore benefit

successful scale translation in STRs where the Bach impeller is used and should be considered to inform future biopharmaceutical production processes.

2. Materials and Methods

2.1 Bioreactor Set-up

All measurements were conducted in a dished bottom, unbaffled, cylindrical vessel made of acrylic, which was manufactured to mimic the dimensions of the commercially available UniVessel 1L Glass bioreactor manufactured by Sartorius (tank height H=180 mm, tank diameter T=110 mm). Throughout all experiments, working volumes of V_w=1,000, 1,250 and 1,500 mL were used, corresponding to liquid heights to tank diameter ratios of H_L/T≈1, 1.25 and 1.5, respectively. The vessel was placed in a water-filled acrylic trough to minimize light refraction due to the curvature of its cylindrical surface. The motor was connected to an Ultra 3000 Servo drive and controlled using the Ultraware software (Rockwell Automation, WI, USA). Two impeller-off-bottom clearances, C, were investigated, C≈0.33T and 0.55T. The off-bottom clearance C was defined as the distance between the bottom line of the Bach impeller blades and the bottom of the tank. A NET iCube camera (NET, Germany) mounted on an adjustable arm was placed to the side of the vessel and used to capture the suspension and mixing processes. A uniform illumination of the vessel was ensured by a white LED panel placed at the back of the vessel on the opposite side of the camera.

2.2 Impeller Designs

All impellers were 3D-printed (selective laser sintering, SLS) in nylon (PA2200, 3DPrint UK, London, UK) using a Formiga P100 machine (Electro Optical Systems, Krailing, Germany). To carry out PIV measurements additional transparent impellers were 3D-printed using stereolithography (SLA) of a clear resin (GPLCL04) in a Form 3 machine (Formlabs, Somerville, MA, USA). Upon printing, The SLA items were polished with wetted sandpaper (800 grit) to smoothen out the surfaces of the blades. A clear lacquer was sprayed onto the items in fine layers under the fume hood to completely fill the left surface scratches. The impellers were then left to dry under the fume hood overnight.

The Bach impeller design and dimensions were provided by Cellmotions, Inc. (Hamilton, Ontario, Canada). Three impeller-to-tank diameter ratios were investigated D/T=0.33, 0.44, and 0.52, and their

dimensions are summarized in Table 1. Two additional axial flow impellers were studied for comparison (Figure 1, B, C): a 3-Blade Segment (3BS) impeller (blade angle α=45°), which is commonly employed in the Sartorius UniVessel Bioreactor System for mammalian cell cultures (*D/T=0.44*); and a marine impeller that is used in the Mobius CellReady bioreactor series (Merck Millipore), and which was scaled down to *D*/*T*=0.44 to ensure comparability with the 3BS impeller. Both impellers worked in up-pumping mode (clockwise rotation).

A
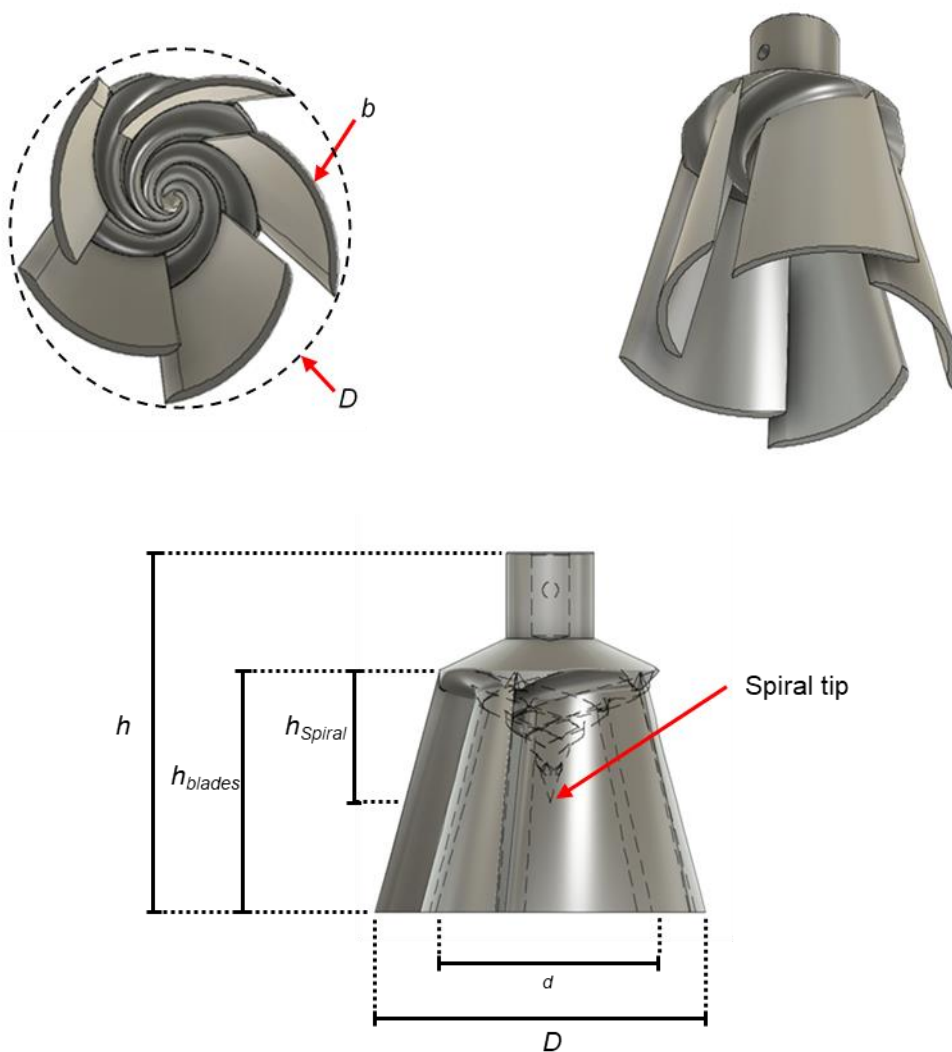
B
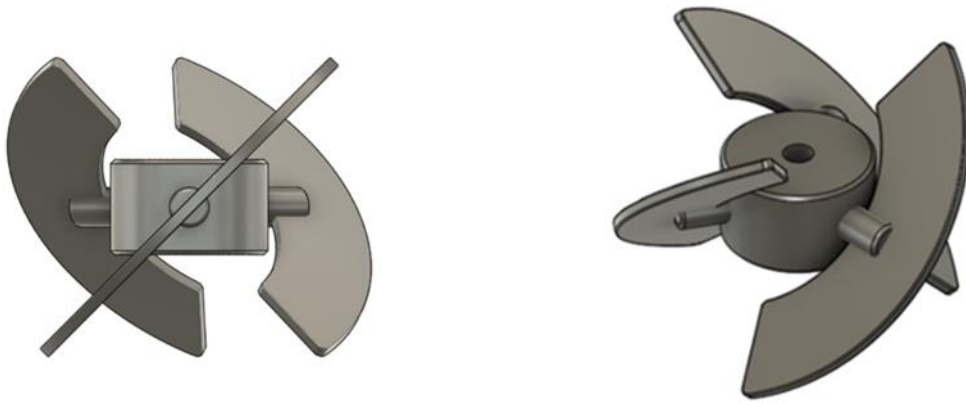
C

Figure 1: Bottom, side, and isometric views of A) Bach impeller, B) 3-Blade segment (3BS) impeller, C) marine impeller

Table 1: Summary of impeller dimensions for diameter D, blade thickness b, and height h

| | Bach | Bach | Bach | 3BS | Marine |
	D/T=0.33	*D/T=0.44*	*D/T=0.52*	*D/T=0.44*	*D/T=0.44*
D [mm]	36.3	48.0	57.2	48.0	48.0
d [mm]	23	30.3	36.2	-	-
b [mm]	0.95	1.26	1.5	1.5	0.6
h [mm]	34.7	46.0	54.6	38.4	10.2
h_{blades} [mm]	23.3	30.9	36.7	-	-
h_{spiral} [mm]	12.8	16.9	20.1	-	-

2.3 Power Consumption

The ungassed impeller power inputs at different rotational speeds were measured with an air bearing system using a digital force gauge (DFG55-10, Omega Engineering, Manchester, UK, sensitivity range 5-500 N) placed at a distance l=45 mm from the vessel axis. The gauge was mounted on a static scaffold surrounding the vessel that was in turn placed on the air-bearing. The air-bearing was supplied with air through a silicon tubing at a constant pressure of 0.2 bar that prevented self-rotation but still ensured smooth motion of the vessel upon impeller agitation. The torque, M, generated by the impeller was obtained by multiplying the distance of the force gauge from the impeller axis, l, times the force, F, applied by a rotating rod rigidly mounted on the vessel on the force gauge element. The measurements (10 per second) were averaged over a period of 60 s with n=3 repeats per condition. Prior to the start of each measurement, the gauge was tared and the fluid was allowed to reach steady state for 60 s to minimize measurement fluctuations. All measurements were conducted at room temperature (RT=22.5 °C) in MilliQ water or MilliQ water-glycerol (99+%, Fisher Scientific, UK) mixtures. The addition of glycerol (0-100%) allowed to determine the power number at low Reynolds numbers (Re, Equation 1) through the increase of the fluid viscosity (~1 cP to ~900 cP). The temperature of the working fluid was monitored before each experiment with a thermometer.

$$Re = \frac{N D^2 \rho_L}{\mu} = \frac{N D^2}{v} \tag{1}$$

Where μ is the dynamic viscosity of the liquid, v is the kinematic viscosity of the liquid, and ρ_L is the liquid density. Three samples (10 mL each) of the working solution were taken after each set of measurements and stored in 50 mL Falcon tubes. The dynamic viscosity of the liquid was then analyzed in a Kinexus lab+ rheometer (Netzsch-Gerätebau GmbH, Selb, Germany) at the liquid temperature of the corresponding experiment. The power input, P, and the power number N_P were determined according to Equation 2 and 3, respectively.

$$P = 2 \pi N M \tag{2}$$

$$N_P = \frac{P}{\rho_L \, N^3 \, D^5} \tag{3}$$

The power input per unit volume P/V as a function of impeller speed (rpm) was fitted using a power function of the form f(x)=a x^b. To estimate the P/V in the turbulent regime, a linear curve fitting was performed (Re>1.5 x 10^4). To fit the power number, N_P, as a function of impeller speed (rpm), a piecewise linear interpolation of the power curve was performed.

2.4 Mixing Time & Suspension Speed

2.4.1 Mixing Time

The Dual Indicator System for Mixing Time (DISMT) was used to characterize mixing time as described in an earlier publication from the research group (Rodriguez et al., 2014). Indicator stock solutions were prepared in 70%-EtOH at a concentration of 1.52 mg mL^{-1} (Methyl Red, MR) and 1.38 mg mL^{-1} (Thymol Blue, TB), and subsequently added to Milli-Q water at a concentration of 4.26 mL L^{-1} (MR) and 4.67 mL L^{-1} (TB). This working solution was then added to the vessel and fully mixed by the impeller until it reached a bright red color. At this stage, the impeller speed was set, and the mixing experiment was started by inserting a stoichiometric amount of 0.75 M NaOH at the free surface through an inlet in the reactor lid using a pipette. The mixing process was monitored by a camera with an image acquisition frame rate of 10 Hz. Image acquisition was stopped when full mixing was visually observed (working solution turning fully yellow with no red or green color traces left over, pH≈7.0), or after a maximum duration of three minutes. Subsequently, the same stochiometric amount of 0.75M HCl was added to the working solution to prepare for a new measurement. The working solution was replaced after a maximum of six measurements to ensure freshness of the reaction and reproducible color changes. Mixing was investigated for N=25–150 rpm with 25 rpm increments and each condition was repeated three times (n=3). Images were then analyzed using a purposely written MATLAB code, where the mixing time was defined as the time necessary to achieve 95% of all pixels being mixed to a degree of 95% (Rodriguez et al., 2014).

2.5.1 Suspension Speed

A total of three different microcarriers were used in the suspension experiments and their characteristics are summarized in Table 2. The microcarriers can be classified by their specific density into three categories, namely, light (≈1.0, like water), intermediate (≈1.1), and heavy (≈1.2), of which the light and intermediately heavy microcarriers are commonly used in cell culture protocols. The PMMA beads (i.e. heavy) are microspheres that have been included in these studies to complement the range of specific densities but are not suitable for cell culture unless coated with a matrix. Suspension of microcarriers was assessed at increasing speeds with the microcarriers being completely settled at the bottom of the reactor at the beginning of each experiment. Side view images of the reactor were recorded with a frame rate of 2 Hz for 3-5 min per condition. Depending on the microcarrier type, impeller speeds between N=10–300 rpm were investigated and post-processed using a purposely written MATLAB code. The suspension speed, N_H, and the suspension number, N_{tH}, were determined from the impeller speed and time required to homogenize the microcarrier concentration to a degree of 90% across the reactor side view (Samaras et al., 2019). A piecewise cubic hermite interpolating polynomial (PCHIP) function was applied to the data to derive the impeller speeds required to homogenize the microcarriers to certain degrees (e.g., 10%, 90%). To determine the suspension number, the suspension homogeneity as a function of time was fitted with a sigmoidal function and a threshold of 95% was selected.

Table 2: Summary of microcarrier types used in this study and their characteristics

	Plastic Plus	**Hillex**	**PMMA**
Category / Specific density [-]	Light / 1.03	Intermediate / 1.11	Heavy / 1.19
Manufacturer	Pall / Sartorius	Pall / Sartorius	Bangs Laboratories
D_{50} [μm]	170	180	165
Porosity	Non-porous	Microporous	Non-porous
Material	Polystyrene	Polystyrene modified with cationic amine	Poly(Methyl Methacrylate)
Charge	No charge	+	No charge

Amount investigated			
(dry weight) [g L^{-1}]	10	10	10

2.6 Velocity Flow field and Flow Number

A green diode laser, with a maximum power output >500 mW and wavelength λ=532 nm, was used for the two-dimensional (2D) particle image velocimetry experiments, together with a cylindrical lens, an intensified NanoSense MKII camera (Dantec Dynamics A/S, Denmark) and a timing box. A vertical laser sheet of approximately 1 mm thickness was produced to measure the radial and axial velocity components. To seed the flow, rhodamine-coated polymethyl methacrylate spheres (20-50 µm, Dantec Dynamics A/S) were used. The camera was equipped with a 570 nm orange light cut-off filter to reduce laser light reflections from the impeller and the acrylic vessel. The refractive index (RI) of the working solution was matched to the used materials for vessel and impeller ($n\approx$1.491 for acrylic (Nguyen et al., 2004)). The RI of MilliQ water was adjusted through the addition of potassium iodide (KI) salt and glycerol, at a concentration of 294:412:294 ($H_2O:KI:C_3H_8O_3$) by weight. The resulting aqueous solution exhibited an RI of $n\approx$1.461 (measured using an optical refractometer, ABBE 5, Bellingham+Stanley Ltd., UK) which was sufficiently high to eliminate potential error sources from refraction and reflection that arise at the solid-liquid interfaces. Lastly, small amounts of sodium thiosulfate were added to prevent yellowing of the solution. The RI matched working solution showed both an increased density ρ_{RI}=1,542 kg m^{-3}, and dynamic viscosity μ=3.94 x 10^{-3} Pa s, at T=22.5 °C, corresponding to a kinematic viscosity of v=2.55 x $10^{-6}\,m^2\,s^{-1}$.

A four-pass adaptive correlation analysis with an initial interrogation window of 128 x 128 pixels and a final window size of 16 x 16 pixels was applied to all images using PIVlab open-source software (Thielicke and Stamhuis, 2014). A final resolution of 8 x 8 pixels was achieved through a 50% interrogation area overlap, corresponding to a spatial resolution of ~1 mm^2. PIVlab was further employed for the derivation of the instantaneous velocity profiles. Additional data post processing was carried out using a purposely written MATLAB code (Mathworks, USA).

A cylindrical coordinate system is used, where the radial, axial, and azimuthal coordinates are indicated in this work by r, z, and θ respectively. The system's origin is in the center of the vessel

bottom. The volumetric fluid flow rates of the Bach impellers have been determined using the ensemble-averaged radial, $\overline{U_r}$, and axial, $\overline{U_z}$, fluid velocity components from 10 impeller revolutions (corresponding to ~1,000 – 4,000 instantaneous velocity fields depending on the impeller speed and size) at Re=1 x 10^3 – 6 x 10^3. The ensemble-averaged radial ($\overline{U_r}$) and axial ($\overline{U_z}$) fluid velocity components of the benchmark impellers were estimated by averaging phase-resolved datasets (400 velocity fields each) obtained at an angular resolution of 3°-14° for both the marine and 3BS impeller. The ensemble-averages were estimated from datasets of 2,800 and 3,200 instantaneous velocity fields for the marine and 3BS impeller, respectively. The local dissipation rate of kinetic energy (ε, EDR) was estimated via the dimensional method from Equation 6 (Ducci and Yianneskis, 2005; Wu and Patterson, 1989).

$$\varepsilon = A\frac{q^{\frac{3}{2}}}{\Lambda} \tag{4}$$

Where A is a constant (=0.85), Λ is the integral length scale estimated as 0.1 D, and q is the kinetic energy (KE) defined in Equation 7 to consider the anisotropy of the flow:

$$q = \frac{1}{2}(u_r'^2 + u_z'^2 + u_w'^2) \tag{5}$$

Where u_r', u_z', u_w' denote the ensemble-averaged standard deviation of the radial, axial, and tangential velocity components, respectively, and where the third term, u_w', is estimated from the average of radial and axial velocity components:

$$u_w' = \sqrt{\frac{u_r'^2 + u_z'^2}{2}} \tag{6}$$

It should be noted that in this study the standard deviation quantities mentioned above include both the turbulent and pseudo-turbulent fluctuations determined by the blade passage.

The inlet and outlet volume rate fluxes across the impeller swept region were obtained by integrating the velocity components over the surface of a hypothetical cylinder encasing the impeller. The resulting volume flow rate, Q, from the surface integrals was used to define the dimensionless flow number, N_Q, according to Equation 7.

$$N_Q = \frac{Q}{N D^3} \tag{4}$$

Lastly, the impeller pumping efficiency (PE) was defined as the ratio of N_Q and N_P (Equation 8).

$$PE = \frac{N_Q}{N_P} \tag{5}$$

2.7 Statistics

For comparisons among multiple groups, one-way analysis of variance (ANOVA) was used with post hoc Tukey's and Scheffé test. A difference of $p < 0.05$ (*), $p < 0.01$ (**), or $p < 0.001$ (***) was considered significant. All statistical tests were performed using OriginPro 2021 (OriginLab).

3. Results & Discussion

3.1 Impeller power number, N_P

In Figure 2, the power curves of the three impellers investigated in this work in clockwise/up-pumping rotation at an off-bottom clearance of $C=0.33T$ are presented for Reynolds numbers from 2 to 30,000. The greatest Reynolds number investigated $Re=30,000$ corresponds to impeller speeds of $N\approx600$ rpm at the 1L scale at ~1 cP, $N\approx220$ rpm at the 10L scale, and $N\approx100$ rpm at the 50L scale. While these are realistic impeller speeds for bioprocessing operations at the respective scales, the power numbers for scales >50L could be re-evaluated at larger scales to include a greater range of Re. The highest power number across the Re range was measured for the 3BS impeller, whose value converged to $N_P=0.74$ at $Re>2 \times 10^4$. This value was ~2.1 times the power number of the Bach impeller ($N_P=0.36$) for the same Re range, despite the 3BS impellers' smaller swept volume. The power number of the marine impeller corresponded to $N_P=0.23$ at comparable Re. These differences in power number were also observed for Re~2,000–6,000, which are commonly present in benchtop sized bioreactors and correspond to 50–150 rpm at the studied impeller diameters in water. The measured turbulent power number for the marine impeller was in good agreement with previously published data obtained using different measurement techniques. For example, van Eikenhorst et al. (van Eikenhorst et al., 2014) determined a power number of 0.22–0.25 (at $Re=2.1 \times 10^4$–2.8×10^4) in an engineering study of lab-scale bioreactors. Kaiser et al. (Kaiser et al., 2011) investigated the Möbius CellReady bioreactor and numerically determined $N_P=0.3$ for the marine impeller. While elephant-ear impellers/pitched blade impellers have been widely investigated in the literature, fewer values can be found with respect to the specific geometry of the 3-blade-segment impeller that is employed in the Sartorius UniVessel reactor. Van Eikenhorst (van Eikenhorst et al., 2014) determined the power number for an unbaffled 2 L single-use bioreactor from Sartorius operating with a dual-3BS impeller

system (blade angles of 30°) used in down-pumping orientation. The combined power number was determined to be 1.9±0.2 (at Re=1.4 x 10^4), indicating that a single impeller had an N_P=0.85±0.1, which is close to the value of N_P≈0.8 determined in this work at the same Reynolds number. The power number of the 3BS at higher Re (>2 x 10^4) is also in good agreement with the value disclosed by the manufacturer from unpublished in-house characterization studies (N_P=0.7) (Sartorius, 2017).
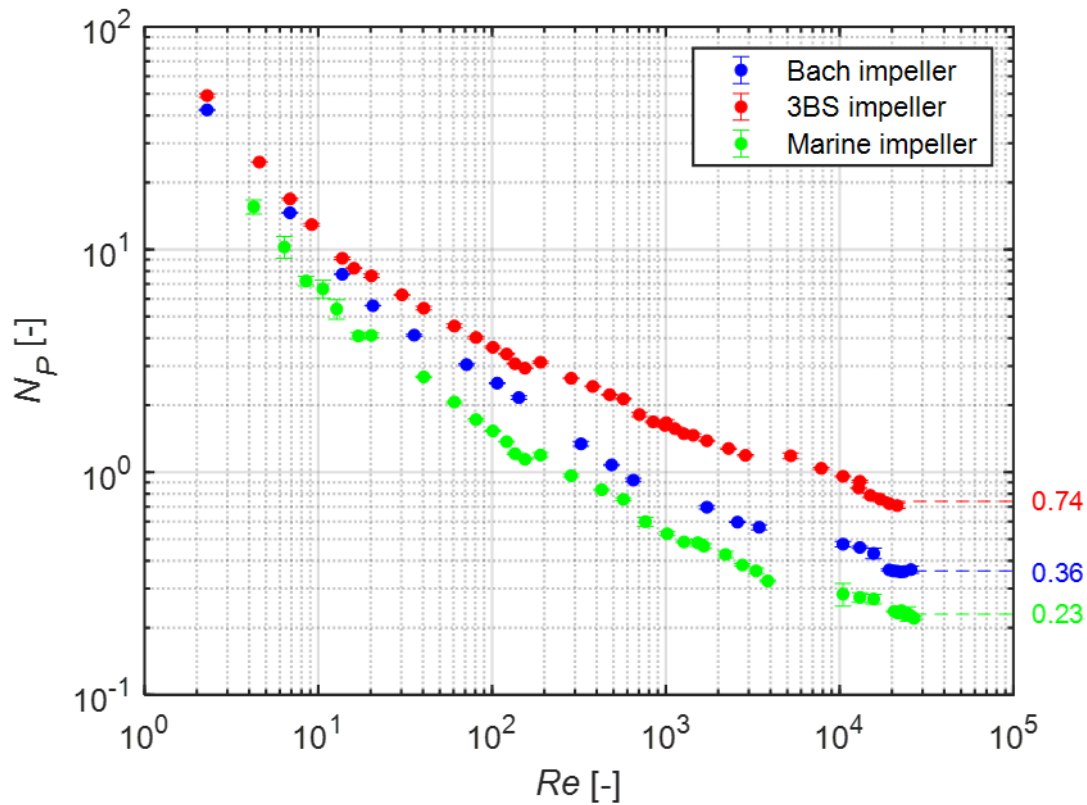

Figure 2: Full power number curves of the three investigated impellers (D/T=0.44) at C=0.33T in up-pumping mode, H_L/T=1. Error bars represent the standard deviation from the mean (SEM) for n=3.

Figure 3 shows the impact of off-bottom clearance, direction of rotation, D/T and H_L/T ratios on the turbulent power numbers (Re>10^4) obtained for the different impellers. For all impellers, the power number did not change to a large extent when the off-bottom clearance was increased to C=0.55T, irrespective of the direction of rotation. However, while changing the direction of rotation of the 3BS and marine impeller did not cause significant changes to the impellers' power number, the power number of the Bach impeller approximately doubled in anticlockwise rotation (Figure 3, A, open blue symbols). This effect is most likely due to the distinct geometric shape and orientation of the impeller

blades, which are streamlined to drive the fluid out of the impeller region in clockwise rotation mode (i.e. up-pumping mode). This efficient flow dynamics is lost when the direction of rotation of the impeller is inverted (Figure 1, A). An investigation on the influence of D/T on the turbulent power number shows that the increase due to anticlockwise rotation was greater for the Bach impeller with a D/T=0.33, and less pronounced but still markedly present at D/T=0.52 (Figure 3, B). The significantly different behavior observed for the Bach impeller with direction of rotation is an interesting new alternative to the standard raising of power input by means of increasing the impeller speed.

Moreover, to investigate whether an increased working volume would have an impact on the power number of the impellers, measurements in the turbulent Reynolds regime were taken at two additional H_L/T ratios of 1.25 and 1.5 (Figure 3, C). It was found that power numbers are significantly affected by the increased H_L/T, with the impellers displaying an increase of N_P of about 10-15% on average for H_L/T=1.25 when compared to H_L/T=1, and of about 15-25% on average for H_L/T=1.5 compared to H_L/T=1. These results are in agreement with Maaß et al. (2010) who found an increase of 13% in power number for a retreat curved impeller when the liquid level was doubled to H_L/T=2 (Maaß et al., 2010). Despite the increase in power number in the turbulent regime, the power input per unit volume decreased with increasing H_L/T ratios for all investigated impellers (Figure 3, D). For example, the Bach impeller's (D/T=0.44) average power input at C=0.33T in the turbulent Re regime increases from P=0.064 W at H_L/T=1.0 to P=0.068 W and P=0.072 W at H_L/T=1.25 and 1.5, respectively. This increase rate of power input is smaller than the volumetric increase from H_L/T=1.0 to 1.25 and 1.5, resulting in a net decrease of P/V. Therefore, the larger the percentage decrease of P/V for an impeller, the more can the power input of an impeller be considered constant and independent of H_L/T. In this sense, the 3BS impeller's power input showed greatest dependency on the working volume (Figure 3, D).
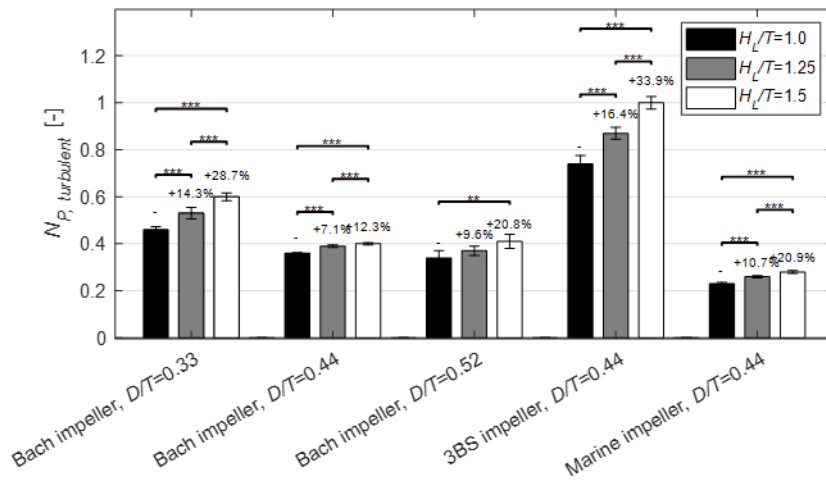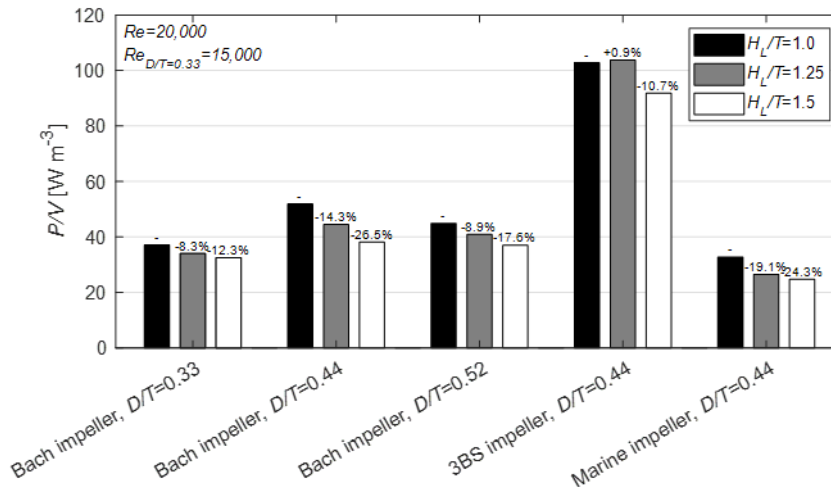
A
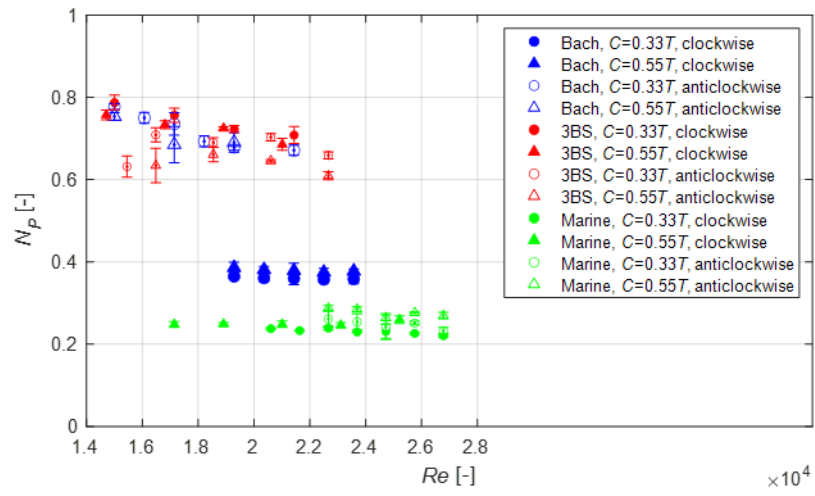
B
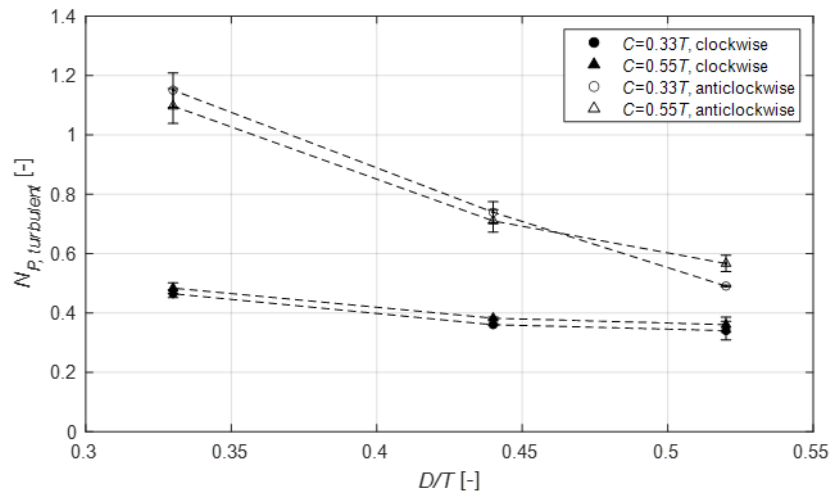
C

D

Figure 3: A) turbulent power numbers of all impellers (D/T=0.44) for different operating conditions, e.g., C=0.55T and anticlockwise rotation. Error bars represent the standard deviation of the means of n=3 times 600 force measurements (60 s at 10 measurements per second). B) average turbulent power number of the Bach impeller at different impeller to tank diameter ratios. Error bars represent the standard deviation of a range of turbulent power numbers from Re=1.5 – 2.5 x 10⁴, or Re=1.0 – 1.5 x 10⁴ for D/T=0.33. C) average turbulent power number of the impellers at different liquid height / tank diameter ratios (H_L/T), C=0.33T. Error bars represent the standard deviation of a range of turbulent power numbers from Re=1.5 – 2.5 x 10⁴, or Re=1.0 – 1.5 x 10⁴ for D/T=0.33. D) Power input

per unit volume at Re=20,000 (Re=15,000 for D/T=0.33) at different liquid height / tank diameter ratios (H_L/T), C=0.33T.

3.2 Mixing

Mixing performance was investigated for a range of impeller speeds (*N*=25-150 rpm) which corresponded to a range of power inputs from ca. 0.03 – 5 W m^{-3} (depending on the power number of the respective impeller) and is shown in Figure 4. Mixing times were recorded for *C*=0.33*T* and *C*=0.55*T* at H_L/*T*=1, and *C*=0.55*T* at H_L/*T*=1.5 (Figure 4, A, B, C, respectively). Across the three studied configurations, the vessel was best mixed by the 3BS impeller, requiring the lowest number of impeller revolutions to achieve full mixing (Figure 4, D, E, F). At low power inputs, t_M was observed to be typically between 75–200 s (i.e. the maximum image acquisition duration). With increasing impeller speeds (*P/V*>0.25 W m^{-3}), t_M decreased asymptotically towards minima of ~10-20 s for the maximum power inputs investigated in this study for all impellers. These observed mixing times compared well with data of van Eikenhorst et al., who also showed that the mixing time approaches 20 seconds at *P/V*=5 W m^{-3} for the 3BS and marine impellers in tanks of similar size (van Eikenhorst et al., 2014). With regards to the determined mixing numbers (Nt_M, number of impeller revolutions necessary to fully mix the tank), a trend of constant Nt_M can be observed for all investigated configurations.

The Bach impeller was studied for two *D/T* ratios (0.52 and 0.44), which showed comparable mixing performance. Notably, a significant reduction in mixing time could be achieved when the Bach impeller was located closer to the free surface of the vessel (*C*=0.55*T* at H_L/*T*=1.0), in comparison to the lower clearance *C*=0.33*T* at H_L/*T*=1.0 (Figure 4, A & D). Likewise, the number of impeller revolutions required to fully mix the volume significantly decreased with the impeller being placed closer to the liquid free surface (Figure 4, E). Despite having the same impeller clearance, *C*, this trend was only observed at H_L/*T*=1.0 and not 1.5 (Figure 4, F). This observation was attributed to the predominantly tangential flow close to the liquid free surface, which was visually supported by the generated mixing maps obtained at *N*=50 rpm for different impeller configurations and presented in Figure 5, A. The mixing maps allow the tracking of the spatial progress of homogenization, revealing regions of high or low mixing times which could be present at specific locations in the tank. From Figure 5, A, it can be seen that for the Bach impeller the maximum average mixing time of ca. 160 s was predominantly around the impeller shaft at *r/T*=±0.15, while the minimum average mixing times

were present in the general bulk fluid at around t_M=40-80 s. Similarly, this was also observed for the Bach impeller at H_L/T=1.5, where t_M averaged at 140-160 s around the impeller shaft (r/T=±0.15) and at 100-120 s for the rest of the vessel, explaining why the increased C did not yield the same improvement as seen for H_L/T=1.0. The Bach impeller's mechanism of agitation in stirred tanks is relatively unconventional and while it might create regions of poor mixing in areas around the shaft, which are not directly affected by the impeller action, the strong vortex that it creates below the impeller can become advantageous in reactors with large H_L/T ratios. If for example the distance between the Bach impeller and the free surface is minimized when selecting C=0.55T at H_L/T=1.0, multiple axial flow impeller-configurations in stirred tanks of >20 L volume could potentially be replaced by a single Bach impeller with access to the fluid below the impeller, though this would have yet to be confirmed experimentally.

The low mixing area was observed to a lesser extent for the benchmark impellers (more so for the marine impeller in comparison to the 3BS impeller) since they generated an upwards pumping axial flow within the vessel which directly acted on the region around the shaft. The marine impeller displayed a region of slower mixing near the free surface (on average 80 s vs. 40 s for the same region in the 3BS impeller) due to its lower power input and therefore weaker axial flow when compared to the 3BS impeller (Figure 5, B).
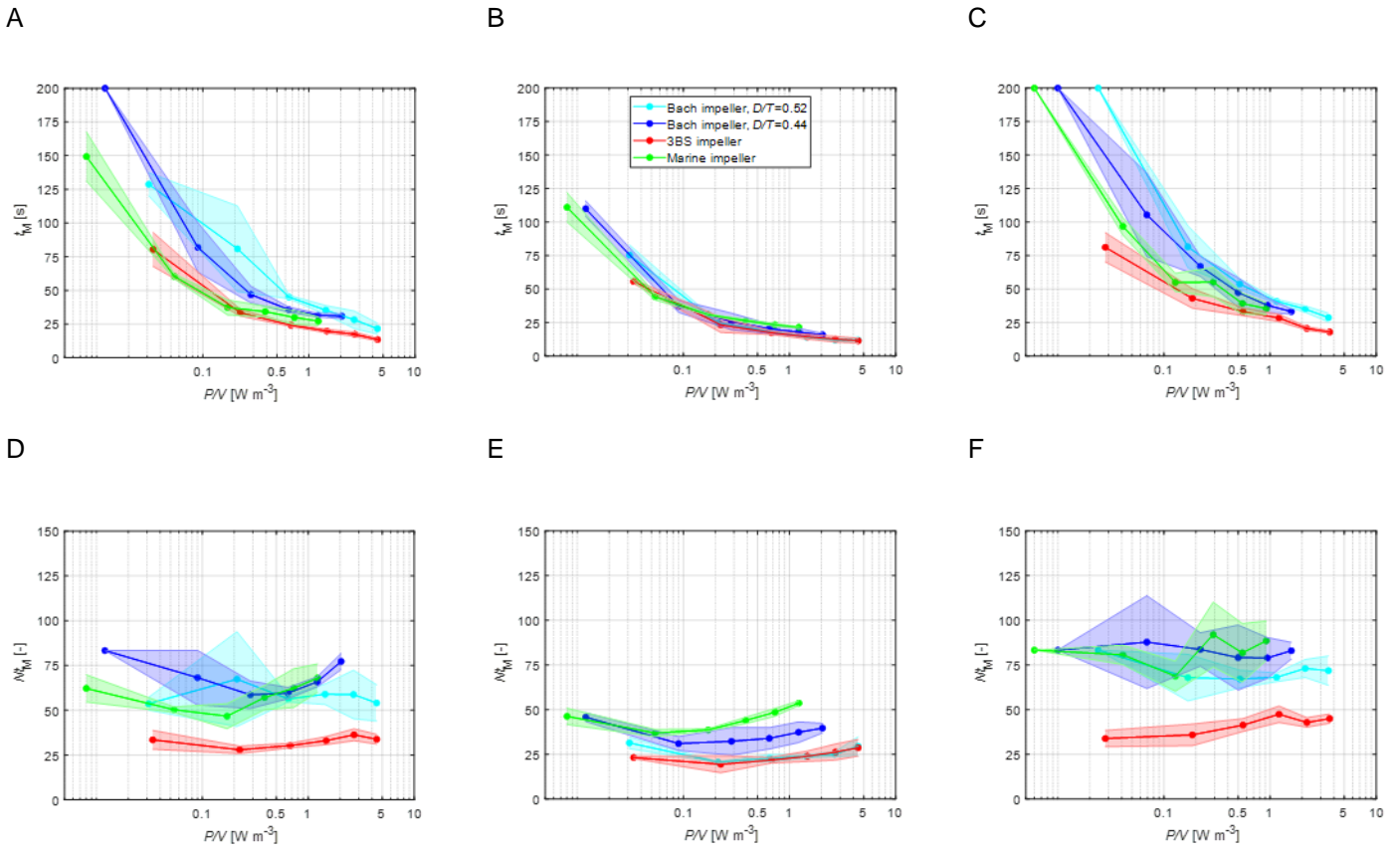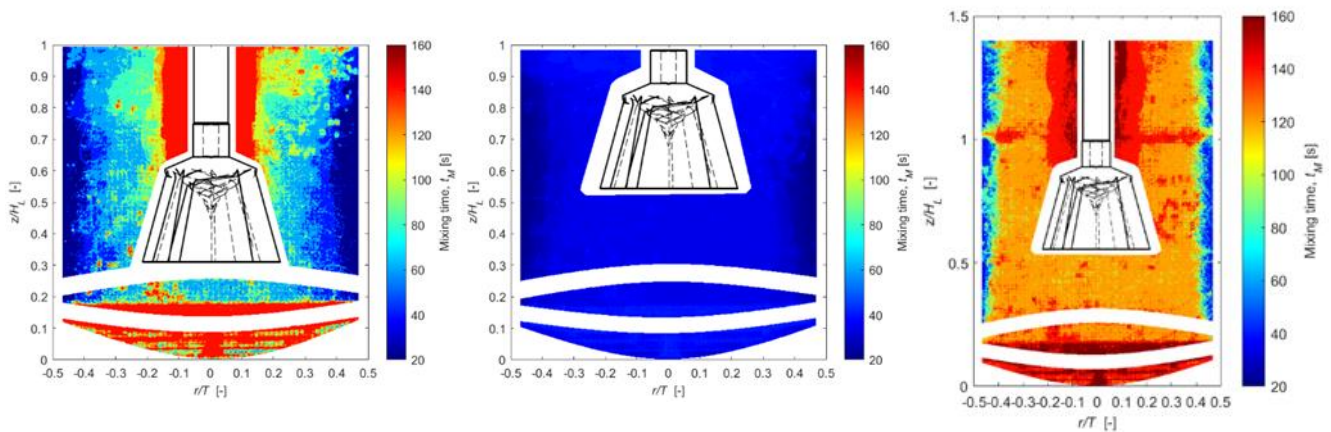
Figure 4: Mixing time and mixing number of Bach impeller, 3BS and marine impellers. A & D) C=0.33T, H_L/T=1.0; B & E) C=0.55T, H_L/T=1.0; C & F) C=0.55T, H_L/T=1.5. The colored surfaces around the collected data points represent the standard deviation of n=3 measurements.
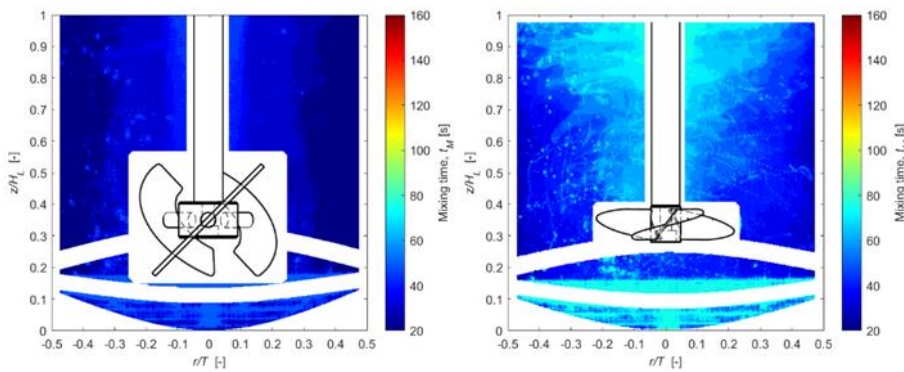
A

B

Figure 5: Mixing maps displaying the average mixing time at N=50 rpm. A) Bach impeller D/T=0.44 at C=0.33T at H_L/T=1.0, C=0.55T at H_LT=1.0, C=0.55T at H_L/T=1.5 (from left to right). B) Two benchmark impellers (D/T=0.44) at C=0.33T at H_LT=1.0.

3.3. Suspension

The impeller speeds at which different microcarriers types would be homogenized were investigated in the model bioreactor at V_w=1,000 mL (H_L/T=1.0). It can be seen in Figure 6 that, as expected, PlasticPlus microcarriers were suspended at the lowest speed by all impellers in comparison to the higher density microcarrier types. For the lightest microcarrier type the Bach impeller (D/T=0.52) required the lowest average impeller speed, $N_{H,\ 1.03}$=25 rpm (P/V=0.032 W m^{-3}), in comparison to the other impellers tested. The 3BS impeller achieved full suspension at a minimum speed of $N_{H,\ 1.03}$=30 rpm and the marine impeller at $N_{H,\ 1.03}$=57 rpm, both at approximately twice the power input measured

for the Bach impeller (P/V=0.056 W m^{-3} and P/V=0.079 W m^{-3}, respectively, Figure 6, A). The speeds at which suspension was achieved for the PlasticPlus microcarriers by the two benchmark impellers are in good agreement with the corresponding values reported in the published literature for particles of similar characteristics (Gadelorge et al., 2018; Hupfeld et al., 2014; Lawson et al., 2017; Mizukami et al., 2016).

The use of light microcarriers with a specific density just above that of water ensures suspension at moderate agitation and thus power input. However, the investigation of heavier microspheres and their behavior in suspension is also of great relevance to biochemical engineering applications. For example, the benefits of using biodegradable microcarriers to simplify the primary recovery step (e.g. avoiding significant cell losses which are observed when the enzymatic method is used) are oftentimes described (Muoio et al., 2021). The greater specific density of some biodegradable materials might deter their use in stirred-tank bioreactors (Lam et al., 2017). The ability to suspend a broad range of microcarrier densities is also useful when considering the formation of cell-microcarrier aggregates, an event often reported in bioreactor studies. These aggregates can potentially reach sizes 10 times the diameter of a single microcarrier, affecting mass and volume of particles that must be suspended (Croughan et al., 2016). It is therefore a desirable feature of an impeller to support a range of microcarrier suspensions at moderate power inputs.

Interestingly, the 90%-homogenization speed was similar between the Hillex and PMMA microspheres, even though PMMA spheres are heavier (Figure 6). For example, the Bach impeller homogenized Hillex microcarriers at $N_{H,\ 1.11}$=105 rpm, and required $N_{H,\ 1.19}$=111 rpm for the PMMA particles (the subscript refer to the particles density). On the other hand, the power input required to suspend the MCs off the bottom (10%-homogenization) was greater for the PMMA particles (Figure 6, B-C) and the number of impeller revolutions required to homogenize to 90% was also on average twice as high (Figure 7, A-C). This indicated that once a certain minimum impeller speed was achieved the microcarriers were suspended to 90%, but all impellers required longer time to achieve suspension for the heavier PMMA spheres. Figure 7 shows the required impeller revolutions, Nt_H, to fully (>90%) suspend the microcarriers as a function of impeller speed (primary x-axis) and volumetric power input (secondary x-axis). It is worth noting that in Figure 7 the power input scale is based on a

impeller to vessel diameter ratio of D/T=0.44. All three impellers require the maximum amount of impeller revolutions at their respective N_H, which is followed by a steep decrease in impeller revolutions, mimicking a function f(x)≈x^{-1}. At N=250 rpm, the marine impeller requires 15-25 impeller revolutions, while Bach and 3BS impeller fully suspend after 5-10 revolutions on average. At P/V≈5 W m^{-3}, though, the amount of required impeller revolutions was equally 15-25 for 3BS impeller and 10-20 impeller revolutions for the Bach impeller.

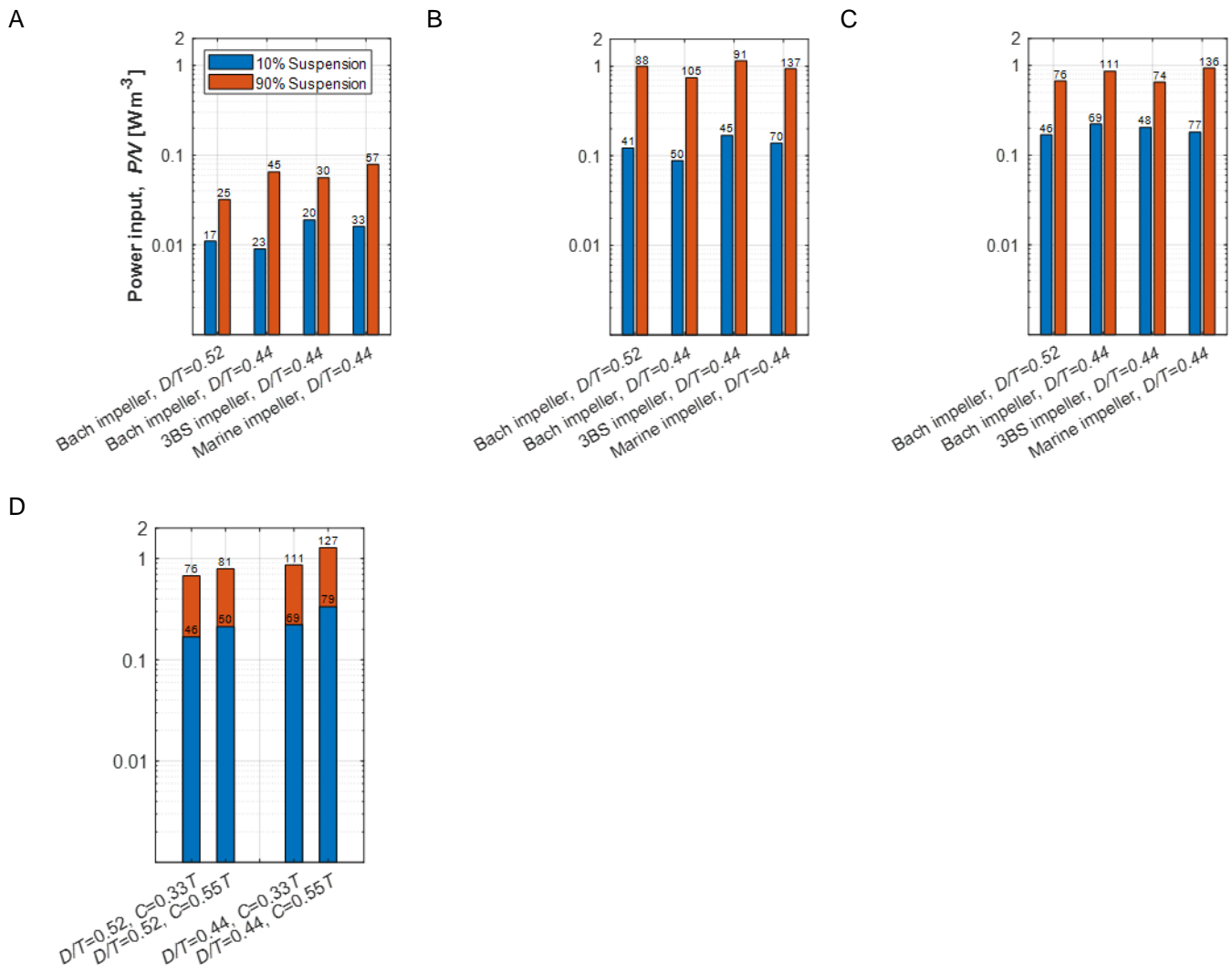

Figure 6: Power input required to homogenize 10% and 90% of A) PlasticPlus microcarriers, B) Hillex microcarriers, and C) PMMA microspheres, at C=0.33T and H_L/T=1.0. D) Power input comparison for Bach impeller for suspension of PMMA microcarriers at C=0.33T vs. C=0.55T. The numbers above bars indicate the respective impeller speeds corresponding to the power input in revolutions per minute (RPM).
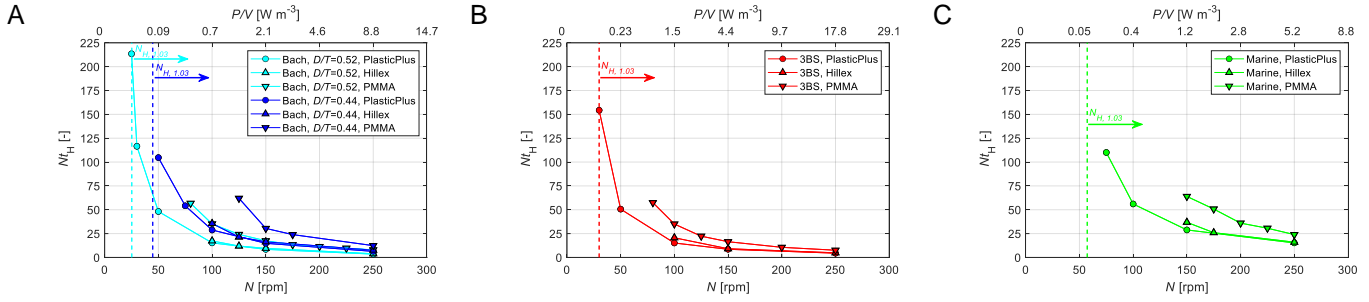
Figure 7: Impeller revolutions, Nt_H, required to reach 95% of final suspension state of >90% at C=0.33T for A) Bach impeller D/T=0.52 and D/T=0.44, B) 3BS impeller, C) marine impeller. The second x-axis in A) shows the volumetric power input of the Bach impeller with D/T=0.44.

3.4. Flow Number & Pumping efficiency

3.4.1 Global flow field

The Particle Image Velocimetry system described in Section 2.6 was used to obtain the ensemble-averaged velocity field shown in Figure 8, where the planar velocity magnitude obtained from the vertical and radial velocity components is denoted as $\overline{U_{rz}}$. Figure 8, A, shows that the Bach impeller produced an upward flow, which was generated by the spiral shaped geometry in the center of the impeller cup. Upon rotation, a vertical vortex that pulled the fluid upwards was created. The fluid was then ejected sidewards through the blade region towards the vessel wall, where it separated at $z/H_L \approx 0.35 \approx C/T$ into two counter-rotating loops in the regions below and above the impeller. The fluid reached its highest velocity $\overline{U_{rz}}=0.25U_{tip}$ at the impeller blades after entry into the impeller cup zone and just prior to being discharged outward. A noticeable region of high fluid velocity was also observed at the tank bottom between z/H_L=0–0.1, where the spiral vortex developed. At radial locations closer to the impeller axis, r/T=0–0.1, the flow field showed small velocities. This might be attributed to the acquisition frequency of the time resolved measurement, 500 Hz at N=191 rpm, which was optimized to resolve the bulk flow field of the reactor but was not high enough to capture the fast axial movement of the particle right below the impeller. This effect is more pronounced at small radii as the seeding particles moved fast in a spiral fashion from one side to the other side of the vortex axis with the adaptive correlation algorithm failing to track the displacement. In agreement with the mixing time results discussed in Figure 5, the entire area above the impeller is also denoted by

24

low fluid movement in the axial and radial direction ($\overline{U_{rz}} \approx 0.1 U_{tip}$), and the flow is predominantly tangential. While this can be mitigated by increasing the off-bottom-clearance of the impeller, it shows again the reliance of proper mixing in STRs on the position of the impeller and the nature of the vortices it creates (Martínez-Delgadillo et al., 2019). Importantly, since the blades themselves are streamlined to the fluid when in up-pumping mode, the spiral part at the center of the impeller is the main element controlling the axial flow in the tank. This is a distinct feature of the novel impeller and explains its comparably low power input.

In contrast, for the conventional impeller designs shown in Figure 8, B-C, the rotating blades act on the fluid and determined the flow pattern present in the vessel. The maximum velocity magnitudes for both impellers, $\overline{U_{rz}}=0.25U_{tip}$, were located at the impeller discharge stream. For the 3BS impeller, the discharge stream covered a greater area in comparison to the marine and Bach impeller. The impeller region can be seen to be the most active zone of the reactor and it can be expected to be the region where most of the kinetic energy is going to dissipate (Ducci and Yianneskis, 2006; Micheletti et al., 2004). The observed fluid velocities are in agreement with previous reports for the marine impeller (Kaiser et al., 2011; Odeleye et al., 2014). The maximum fluid velocity observed for the 3BS impeller is lower than that found by Collignon et al. (Collignon et al., 2010) and Zhu et al. (Zhu et al., 2009) for a down-pumping elephant ear impeller (~0.3-0.4U_{tip}) and an up-pumping elephant ear impeller (0.42U_{tip}), respectively. However, it should be noted that in both the aforementioned studies the reactor included baffles which redirect the flow into the vertical planes, and which have been shown to increase fluid velocities in the radial and axial direction by up to 50% (Atibeni et al., 2013; Fan et al., 2021). The global flow field presented by Zhu et al. (Zhu et al., 2009) shows otherwise equal velocity magnitudes in the bulk flow region, with 0.2-0.3U_{tip}.
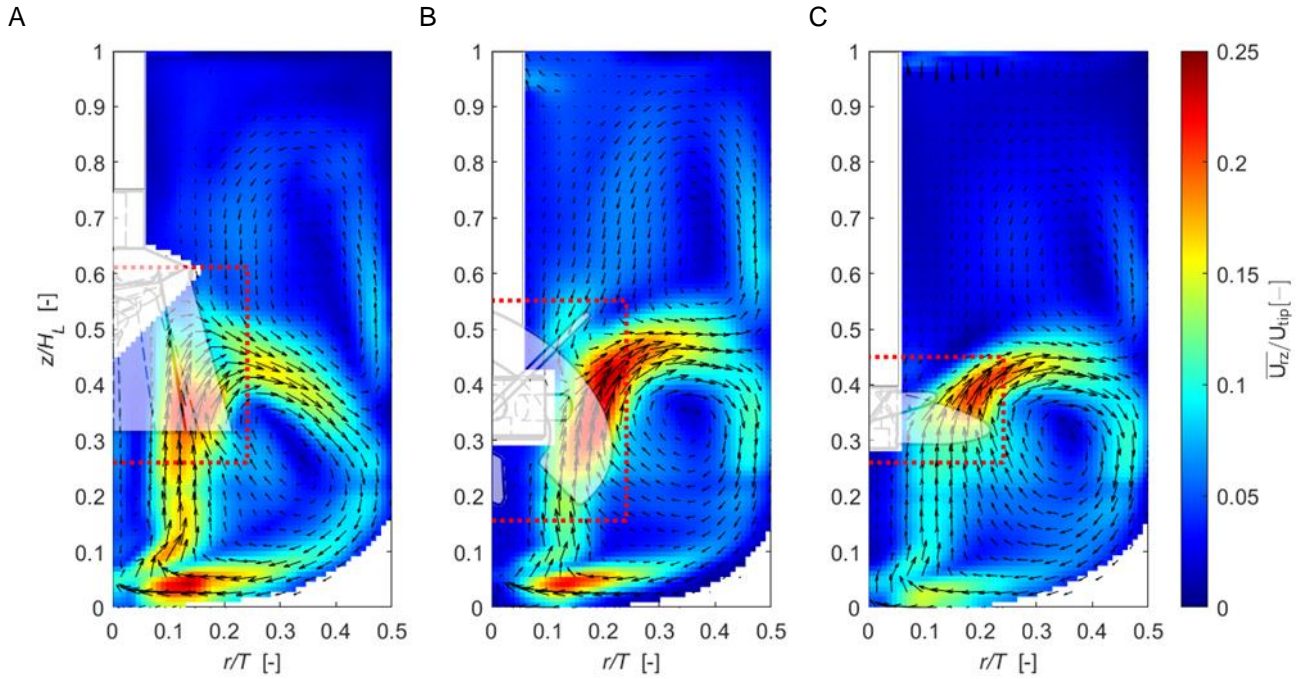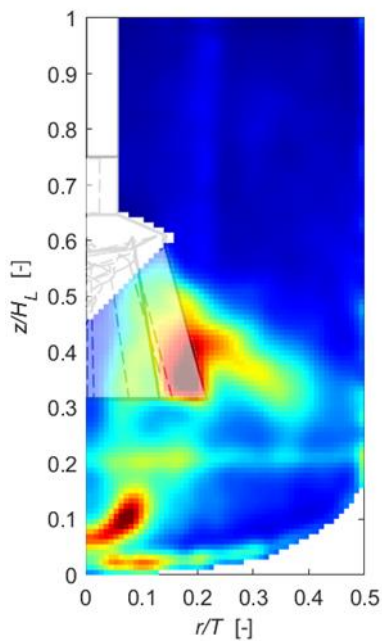
Figure 8: Normalized ensemble-averaged velocity magnitude and contour plot (V$_W$=1 L, H$_L$≈T, N=191 rpm Re≈2,900) at the vertical center plane of the vessel for A) Bach impeller, D/T=0.44, C=0.33T, B) 3BS impeller, C=0.33T, C) marine impeller, C=0.33T. Red dotted line around impellers indicates dimensions of cylinder through which the fluid flow was assessed for the flow number determination.

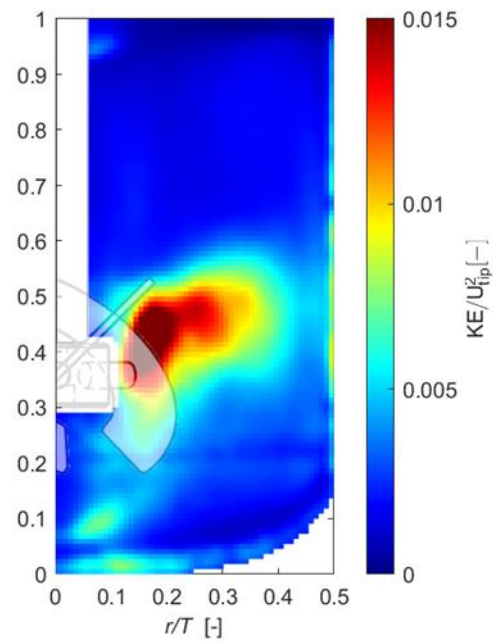### 3.4.2 Kinetic energy and energy dissipation rate

The Particle Image Velocimetry system described in Section 2.6 was additionally used to obtain the ensemble-averaged kinetic energy due to the combined contributions of turbulent and pseudo-turbulent velocity fluctuations and the corresponding dissipation rates shown in Figure 9. These plots are provided only for the Bach and 3BS impeller as these were the one associated to higher velocity fluctuations (at least double than those found in the marine impeller) Figure 9, A-B, show that the kinetic energy associated to velocity fluctuations is highest in the impeller region where the ensemble averaged velocity field showed the greatest velocity magnitudes. The Bach impeller generates peak kinetic energy of KE U_{tip}^{-2}≈0.015–0.02 at the impeller blades where the fluid enters into the impeller cup zones and just prior to being discharged outward. In addition, in comparison to the 3BS impeller, elevated levels of KE were present at the bottom of the vessel, where the fluid vortex is being formed through the action of the central spiral element. For the 3BS impeller, maximum KE$_{max}$≈0.015–0.02U_{tip}^2 were observed as well, although for a greater volume that spans from the impeller blades to r/T≈0.3 with intermediary KE levels of ~0.005-0.1U_{tip}^2 reaching close to the vessel walls at r/T=0.4

(Figure 9, B). The kinetic energy distribution of the 3BS impeller is in agreement with (Zhu et al., 2009), who found maximum KE $U_{tip}^{-2} \approx 0.02\text{-}0.025$ at the edges of both up- and down pumping elephant ear impeller blades. In agreement with the power number described in Figure 2, the 3BS impeller is denoted by higher local values of the dissipation rate (at least 50% higher than the Bach impeller), which confirms that the Bach impeller might be a better option for more shear sensitive cell-lines. As expected, the 3BS impeller is characterized by a localized high dissipation region in proximity of the blade tip, while for the Bach impeller a second region where the central spiral vortex meets the bottom of the tank is present (Figure 9 C-D).
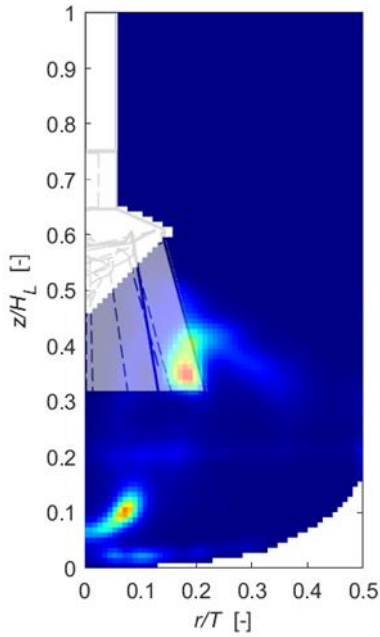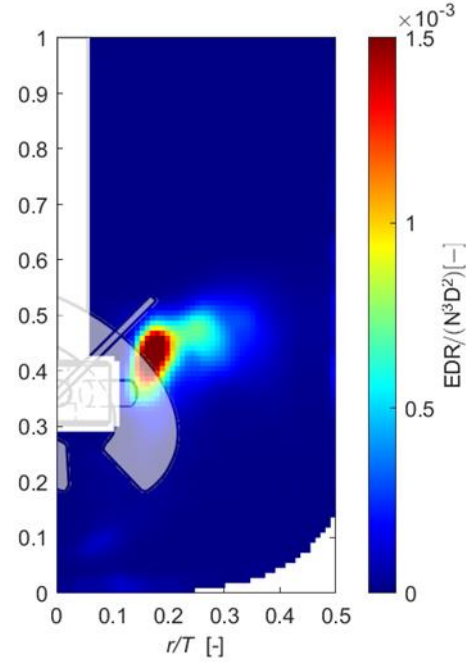
A

B

Figure 9: Normalized ensemble-averaged kinetic energy (KE) and energy dissipation rate contour plots (V_W=1 L, H_L≈T, N=191 rpm / Re≈2,900) at the vertical center plane of the vessel for A & C) Bach impeller, D/T=0.44, C=0.33T, B & D) 3BS impeller, C=0.33T, ~~C & F) marine impeller, C=0.33T.~~

3.4.3 Flow number and Pumping Efficiency

The volume flow rate, Q, was obtained either from the inlet or outlet fluxes within the impeller swept volume. The final value shown in Figure 10, A, was the average of the two, while the error bar corresponds to the difference between the inlet and outlet fluxes. The dimensions of the impeller swept volume are indicated by the red dotted line in Figure 8, A-C). For the Bach impeller, the three D/T ratios have been measured at two clearances C=0.33T and C=0.55T. The measurements showed that the volume flow rate remains mostly identical for the Bach impellers irrespective of the off-bottom clearance. The greatest fluid volume flow rate was produced by the Bach impeller with D/T=0.52, while the Bach impeller with D/T=0.44 and the 3BS impeller reached approximately equal pumping rates. The marine impeller pumped the least amount of fluid, which was expected given its smaller swept volume. At N=191 rpm, it managed to pump Q≈130 mL/s in comparison to Q≈165 mL/s for the Bach (D/T=0.44) and Q≈185 mL/s for the 3BS impeller. As a result of the low fluid displacement by the marine impeller, the flow number was the lowest amongst all tested impellers at N_Q=0.36 at Re≈2,900 (Table 3). The measured flow number for the 3BS impeller was N_Q=0.53, which was similar to the flow numbers calculated for the Bach impeller at the same Re (N_Q=0.41 for

D/T=0.52, N_Q=0.47 for *D/T*=0.44, and N_Q=0.52 for *D/T*=0.33). The flow numbers of the benchmark impellers were comparable to those found by Wu et al. (2000, 2006) and Jaworski, Nienow and Dyster (1996) for a variety of axial flow pitched blade turbines (Jaworski et al., 1996; Wu et al., 2006; Wu and Pullum, 2000).

Of all investigated impellers, the 3BS displayed the lowest pumping efficiency, *PE*, due to its large power number that does not result in increased pumping capacity (Figure 10, B). Due to the marine impellers very low power number, the *PE* was highest at the investigated range of *Re* despite pumping the least amount of volume at *D/T*=0.44 and despite having the lowest flow number. The *PE* of the Bach impeller at the investigated *Re* was approximately equal irrespective of the impeller size.
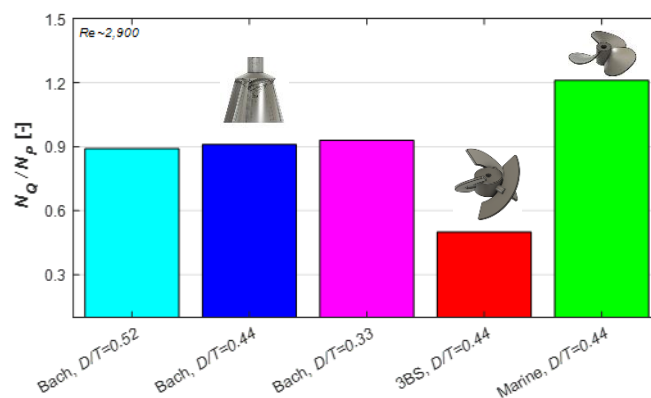
A
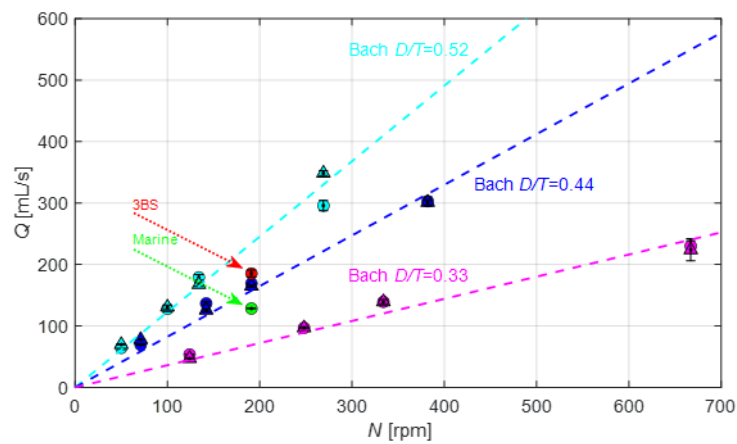
B

Figure 10: A) Volume flow rate, Q, through the impeller swept volume. Error bars indicate the mean difference between measured inflow and outflow of the impeller region. Circular symbols represent data points obtained at C=0.33T. Triangular symbols represent data points obtained at C=0.55T. The

dotted lines represent linear curve fittings of the mean Q of both clearances for the respective Bach impellers. B) Pumping efficiency at Re≈2,900 for the investigated impellers.

4. Conclusions

In this study, a novel impeller was characterized in detail in different reactor configurations and compared with two benchmark axial flow impellers. The Bach impeller exhibited a low power number compared to its size in clockwise rotation (up-pumping mode), mainly because of the streamlined blades with reduced drag. At the 1 L scale the impeller additionally displayed effective mixing and suspension, with suspension speeds of >30-50 rpm for commercially available light microcarriers and efficient mixing speeds at >50 rpm. To further improve mass transfer and overall microcarrier homogeneity during cell culture, it may hence be recommendable to operate the Bach impeller at speeds ranging from 50 to 75 rpm. It was shown that while the marine impeller had the greatest pumping efficiency at N_Q/N_P≈1.2, its design is less capable of suspending microcarriers, requiring higher impeller speeds and more impeller revolutions. The 3BS impeller demonstrated to mix the reactor volume most effectively, but also displayed the worst pumping efficiency of N_Q/N_P≈0.5 due to its large power input. With a pumping efficiency of N_Q/N_P≈0.9, the Bach impeller may be a viable alternative that manages to effectively mix and suspend at low power inputs.

The Bach impeller is a mixing device that, in contrast to the traditional axial flow impellers, does not induce fluid motion by the direct action of the blades but through a spiral at the center of its cup. As such, the fluid follows a pre-defined trajectory that consists of being axially pulled towards the impeller and being expelled sideward through the vane openings before being pulled towards it again. Due to the impeller's mixing mechanism, it may be less restricted by changes in off-bottom clearance and as such, advantages of the design may become more evident for reactors at larger scale. In future studies it might be useful to investigate the size of the "area of influence" of the Bach impeller for a range of impeller speeds, to evaluate the maximum feasible distance to the tank bottom. Reducing the number of impellers in large tanks could reduce the overall energy that is put into the liquid and therefore stress levels across the tank volume, which may be desirable when processing growing organisms such as biological cells. In addition, upcoming studies will aim to characterize in more depth fluid dynamics parameters to inform future users in scale translation.

5. Acknowledgments

6. Nomenclature

6.1. Roman characters

A	Constant, Eq. 6
B	Blade thickness, [mm]
C	Impeller off-bottom clearance
D	Impeller diameter, [m]
D_{50}	Median microcarrier diameter, [μm]
H	Tank height, [m]
h	Impeller height, [mm]
h_{Spiral}	Bach impeller spiral size, [mm]
h_{Blades}	Bach impeller height, [mm]
H_L	Liquid height, [m]
l	Lever arm, [m]
N	Impeller rotational speed, [rpm]
n	Refractive index, [-]
n	Number of experimental repeats, [-]
N_H	Suspension speed, [rpm]
$N_{H, 1.03}$	Suspension speed for microcarrier with specific ρ=1.03, [rpm]
$N_{H, 1.11}$	Suspension speed for microcarrier with specific ρ=1.11, [rpm]

$N_{H,\ 1.19}$	Suspension speed for microcarrier with specific $\rho=1.19$, [rpm]
N_{JS}	Just suspended impeller speed, [rpm]
N_P	Power number, [-]
N_Q	Flow number, [-]
Nt_H	Suspension number, [-]
Q	Fluid volume flow rate, [m^3 s^{-1}]
q	Kinetic energy [m^2 s^{-2}]
r	Radial direction distance, [m]
Re	Reynolds number, [-]
RT	Room temperature, [°C]
T	Tank internal diameter, [m]
T	Temperature, [°C]
t_M	Mixing time, [s]
U_{tip}	Impeller tip speed, [m s^{-1}]
$\overline{U_r}$	Ensemble-averaged radial velocity, [m s^{-1}]
$\overline{U_z}$	Ensemble-averaged axial velocity, [m s^{-1}]
$\overline{U_{rz}}$	Ensemble-averaged magnitude of radial and axial velocity components, [m s^{-1}]
$u_r^{'}$	Ensemble-averaged fluctuating velocity component in radial direction, [m s^{-1}]
$u_z^{'}$	Ensemble-averaged fluctuating velocity component in axial direction, [m s^{-1}]
$u_w^{'}$	Ensemble-averaged fluctuating velocity component in tangential direction, [m s^{-1}]
V_W	Working volume, [L]
z	Axial direction distance, [m]

6.2. Greek characters

μ	Dynamic viscosity, [kg m^{-1} s^{-1}]
α	Blade angle, [deg]
θ	Tangential direction and phase angle, [deg]
λ	Wavelength, [nm]

Λ	Integral length scale, [m]
ν	Kinematic viscosity, [m^2 s^{-1}]
ρ_L	Liquid density, [kg m^{-3}]
ε	Kinetic energy viscous dissipation rate, [m^2 s^{-3}]

6.3. Abbreviations

2D	Two dimensional
3BS	3-Blade Segment impeller
3D	Three dimensional
ANOVA	Analysis of Variance
CFD	Computational Fluid Dynamics
EDR	Energy dissipation rate
Gly	Glycerol
KI	Potassium iodide
LED	Light emitting diode
MC / MCs	Microcarrier/s
MilliQ	De-ionized water
MR	Methyl red
PAT	Process automated technology
PCHIP	Piecewise Cubic Hermite Interpolating Polynomial
PE	Pumping efficiency
PIV	Particle Image Velocimetry
PMMA	Poly(methyl methacrylate)
RI	Refractive index
RPM	Revolutions per minute
SLA	Stereo lithographic apparatus
SLS	Selective laser sintering
STR	Stirred tank bioreactor
TB	Thymol blue
KE	Kinetic energy due to turbulence and pseudo-turbulence due to blade passage

7. List of References

Ahsan, T., Nerem, R.M., 2010. Fluid shear stress promotes an endothelial-like phenotype during the early differentiation of embryonic stem cells. Tissue Eng. - Part A 16, 3547–3553. https://doi.org/10.1089/ten.tea.2010.0014

Atibeni, R., Gao, Z., Bao, Y., 2013. Effect of baffles on fluid flow field in stirred tank with floating particles by using PIV. Can. J. Chem. Eng. 91, 570–578. https://doi.org/10.1002/cjce.21652

Bliatsiou, C., Malik, A., Böhm, L., Kraume, M., 2019. Influence of Impeller Geometry on Hydromechanical Stress in Stirred Liquid/Liquid Dispersions. Ind. Eng. Chem. Res. 58, 2537–2550. https://doi.org/10.1021/acs.iecr.8b03654

Böhm, L., Hohl, L., Bliatsiou, C., Kraume, M., 2019. Multiphase Stirred Tank Bioreactors – New Geometrical Concepts and Scale-up Approaches. Chemie-Ingenieur-Technik. https://doi.org/10.1002/cite.201900165

Chalmers, J.J., 2015. Mixing, aeration and cell damage, 30+ years later: What we learned, how it affected the cell culture industry and what we would like to know more about. Curr. Opin. Chem. Eng. https://doi.org/10.1016/j.coche.2015.09.005

Cherry, R.S., 1993. Animal cells in turbulent fluids: Details of the physical stimulus and the biological response. Biotechnol. Adv. https://doi.org/10.1016/0734-9750(93)90043-M

Chisti, Y., 2001. Hydrodynamic damage to animal cells. Crit. Rev. Biotechnol. https://doi.org/10.1080/20013891081692

Collignon, M.L., Delafosse, A., Crine, M., Toye, D., 2010. Axial impeller selection for anchorage dependent animal cell culture in stirred bioreactors: Methodology based on the impeller comparison at just-suspended speed of rotation. Chem. Eng. Sci. 65, 5929–5941. https://doi.org/10.1016/j.ces.2010.08.027

Croughan, M.S., Giroux, D., Fang, D., Lee, B., 2016. Novel Single-Use Bioreactors for Scale-Up of Anchorage-Dependent Cell Manufacturing for Cell Therapies, in: Stem Cell Manufacturing. Elsevier, pp. 105–139. https://doi.org/10.1016/B978-0-444-63265-4.00005-4

de Sousa Pinto, D., Bandeiras, C., de Almeida Fuzeta, M., Rodrigues, C.A.V., Jung, S., Hashimura, Y., Tseng, R.J., Milligan, W., Lee, B., Ferreira, F.C., Lobato da Silva, C., Cabral, J.M.S., 2019. Scalable Manufacturing of Human Mesenchymal Stromal Cells in the Vertical-Wheel Bioreactor System: An Experimental and Economic Approach. Biotechnol. J. 14, 1800716.

https://doi.org/10.1002/biot.201800716

Ducci, A., Yianneskis, M., 2006. Turbulence kinetic energy transport processes in the impeller stream of stirred vessels. Chem. Eng. Sci. 61, 2780–2790. https://doi.org/10.1016/j.ces.2005.09.020

Ducci, A., Yianneskis, M., 2005. Direct determination of energy dissipation in stirred vessels with two-point LDA. AIChE J. 51, 2133–2149. https://doi.org/10.1002/aic.10468

Fan, Y., Sun, J., Jin, J., Zhang, H., Chen, W., 2021. The effect of baffle on flow structures and dynamics stirred by pitch blade turbine. Chem. Eng. Res. Des. 168, 227–238. https://doi.org/10.1016/j.cherd.2021.01.017

Gadelorge, M., Bourdens, M., Espagnolle, N., Bardiaux, C., Murrell, J., Savary, L., Ribaud, S., Chaput, B., Sensebé, L., 2018. Clinical-scale expansion of adipose-derived stromal cells starting from stromal vascular fraction in a single-use bioreactor: proof of concept for autologous applications. J. Tissue Eng. Regen. Med. 12, 129–141. https://doi.org/10.1002/term.2377

Hanga, M.P., Ali, J., Moutsatsou, P., Raga, F.A., Hewitt, C.J., Nienow, A., Wall, I., 2020. Bioprocess development for scalable production of cultivated meat. Biotechnol. Bioeng. bit.27469. https://doi.org/10.1002/bit.27469

Hupfeld, J., Gorr, I.H., Schwald, C., Beaucamp, N., Wiechmann, K., Kuentzer, K., Huss, R., Rieger, B., Neubauer, M., Wegmeyer, H., 2014. Modulation of mesenchymal stromal cell characteristics by microcarrier culture in bioreactors. Biotechnol. Bioeng. 111, 2290–2302. https://doi.org/10.1002/bit.25281

Jaszczur, M., Młynarczykowska, A., Demurtas, L., 2020. Effect of impeller design on power characteristics and Newtonian fluids mixing efficiency in a mechanically agitated vessel at low reynolds numbers. Energies 13, 640. https://doi.org/10.3390/en13030640

Jaworski, Z., Nienow, A.W., Dyster, K.N., 1996. An LDA Study of the Turbulent Flow Field in a Baffled Vessel Agitated by an Axial, Down-pumping Hydrofoil Impeller. Can. J. Chem. Eng. 74, 3–15. https://doi.org/10.1002/cjce.5450740103

Jossen, V., Schirmaier, C., den Bos, C. van, Siehoff, A., Eibl, D., Herrmann, J., Eibl, R., Kaiser, S.C., Tappe, A., 2014. Modification and qualification of a stirred single-use bioreactor for the improved expansion of human mesenchymal stem cells at benchtop scale. Pharm. Bioprocess. 2, 311–322. https://doi.org/10.4155/pbp.14.29

Kaiser, S.C., Eibl, R., Eibl, D., 2011. Engineering characteristics of a single-use stirred bioreactor at

bench-scale: The Mobius CellReady 3L bioreactor as a case study. Eng. Life Sci. 11, 359–368. https://doi.org/10.1002/elsc.201000171

Klöckner, W., Diederichs, S., Büchs, J., 2014. Orbitally shaken single-use bioreactors. Adv. Biochem. Eng. Biotechnol. 138, 45–60. https://doi.org/10.1007/10_2013_188

Lam, A.T.L., Li, J., Toh, J.P.W., Sim, E.J.H., Chen, A.K.L., Chan, J.K.Y., Choolani, M., Reuveny, S., Birch, W.R., Oh, S.K.W., 2017. Biodegradable poly-ε-caprolactone microcarriers for efficient production of human mesenchymal stromal cells and secreted cytokines in batch and fed-batch bioreactors. Cytotherapy 19, 419–432. https://doi.org/10.1016/j.jcyt.2016.11.009

Lawson, T., Kehoe, D.E., Schnitzler, A.C., Rapiejko, P.J., Der, K.A., Philbrick, K., Punreddy, S., Rigby, S., Smith, R., Feng, Q., Murrell, J.R., Rook, M.S., 2017. Process development for expansion of human mesenchymal stromal cells in a 50 L single-use stirred tank bioreactor. Biochem. Eng. J. 120, 49–62. https://doi.org/10.1016/j.bej.2016.11.020

Loubière, C., Delafosse, A., Guedon, E., Toye, D., Chevalot, I., Olmos, E., 2019. Optimization of the Impeller Design for Mesenchymal Stem Cell Culture on Microcarriers in Bioreactors. Chem. Eng. Technol. https://doi.org/10.1002/ceat.201900105

Maaß, S., Metz, F., Rehm, T., Kraume, M., 2010. Prediction of drop sizes for liquid-liquid systems in stirred slim reactors-Part I: Single stage impellers. Chem. Eng. J. 162, 792–801. https://doi.org/10.1016/j.cej.2010.06.007

Martínez-Delgadillo, S.A., Alonzo-Garcia, A., Mendoza-Escamilla, V.X., González-Neria, I., Antonio Yáñez-Varela, J., 2019. Analysis of the turbulent flow and trailing vortices induced by new design grooved blade impellers in a baffled tank. Chem. Eng. J. 358, 225–235. https://doi.org/10.1016/j.cej.2018.10.015

Micheletti, M., Baldi, S., Yeoh, S.L., Ducci, A., Papadakis, G., Lee, K.C., Yianneskis, M., 2004. On spatial and temporal variations and estimates of energy dissipation in stirred reactors. Chem. Eng. Res. Des. 82, 1188–1198. https://doi.org/10.1205/cerd.82.9.1188.44172

Mizukami, A., Fernandes-Platzgummer, A., Carmelo, J.G., Swiech, K., Covas, D.T., Cabral, J.M.S., da Silva, C.L., 2016. Stirred tank bioreactor culture combined with serum-/xenogeneic-free culture medium enables an efficient expansion of umbilical cord-derived mesenchymal stem/stromal cells. Biotechnol. J. 11, 1048–1059. https://doi.org/10.1002/biot.201500532

Muoio, F., Panella, S., Lindner, M., Jossen, V., Harder, Y., Moccetti, T., Eibl, R., Müller, M., Tallone,

T., 2021. Development of a biodegradable microcarrier for the cultivation of human adipose

stem cells (Hascs) with a defined xeno-and serum-free medium. Appl. Sci. 11, 1–27.

https://doi.org/10.3390/app11030925

Nguyen, T.T., Biadillah, Y., Mongrain, R., Brunette, J., Tardif, J.C., Bertrand, O.F., 2004. A method for

matching the refractive index and kinematic viscosity of a blood analog for flow visualization in

hydraulic cardiovascular models. J. Biomech. Eng. 126, 529–535.

https://doi.org/10.1115/1.1785812

Odeleye, A., Lye, G.J., Micheletti, M., 2013. Engineering characterisation of single-use bioreactor

technology for mammalian cell culture applications. BMC Proc. 7, P91.

https://doi.org/10.1186/1753-6561-7-S6-P91

Odeleye, A.O.O., Marsh, D.T.J., Osborne, M.D., Lye, G.J., Micheletti, M., 2014. On the fluid dynamics

of a laboratory scale single-use stirred bioreactor. Chem. Eng. Sci. 111, 299–312.

https://doi.org/10.1016/j.ces.2014.02.032

Rafiq, Q.A., Coopman, K., Hewitt, C.J., 2013. Scale-up of human mesenchymal stem cell culture:

current technologies and future challenges. Curr. Opin. Chem. Eng. 2, 8–16.

https://doi.org/10.1016/J.COCHE.2013.01.005

Rodriguez, G., Anderlei, T., Micheletti, M., Yianneskis, M., Ducci, A., 2014. On the measurement and

scaling of mixing time in orbitally shaken bioreactors. Biochem. Eng. J. 82, 10–21.

https://doi.org/10.1016/j.bej.2013.10.021

Rotondi, M., Grace, N., Betts, J., Bargh, N., Costariol, E., Zoro, B., Hewitt, C.J., Nienow, A.W., Rafiq,

Q.A., 2021. Design and development of a new ambr250® bioreactor vessel for improved cell

and gene therapy applications. Biotechnol. Lett. 43, 1103–1116. https://doi.org/10.1007/s10529-

021-03076-3

Samaras, J.J., Micheletti, M., Ducci, A., 2019. Suspension and Mixing Characterization of Intermittent

Agitation Modes in DASGIP Bioreactors. Chem. Eng. Technol. ceat.201900069.

https://doi.org/10.1002/ceat.201900069

Sartorius, 2017. UniVessel glass characterization data CC.

Singh, V., 1999. Disposable bioreactor for cell culture using wave-induced agitation. Cytotechnology

30, 149–158. https://doi.org/10.1023/a:1008025016272

Thielicke, W., Stamhuis, E.J., 2014. PIVlab – Towards User-friendly, Affordable and Accurate Digital

Particle Image Velocimetry in MATLAB. J. Open Res. Softw. 2. https://doi.org/10.5334/jors.bl

van Eikenhorst, G., Thomassen, Y.E., van der Pol, L.A., Bakker, W.A.M., 2014. Assessment of mass transfer and mixing in rigid lab-scale disposable bioreactors at low power input levels. Biotechnol. Prog. 30, 1269–1276. https://doi.org/10.1002/btpr.1981

Weyand, B., Israelowitz, M., Von Schroeder, H.P., Vogt, P.M., 2009. Fluid dynamics in bioreactor design: Considerations for the theoretical and practical approach. Adv. Biochem. Eng. Biotechnol. https://doi.org/10.1007/978-3-540-69357-4_11

Wu, H., Patterson, G.K., 1989. Laser-Doppler measurements of turbulent-flow parameters in a stirred mixer. Chem. Eng. Sci. 44, 2207–2221. https://doi.org/10.1016/0009-2509(89)85155-3

Wu, J., Graham, L.J., Nguyen, B., Nabil Noui Mehidi, M., 2006. Energy efficiency study on axial flow impellers. Chem. Eng. Process. Process Intensif. 45, 625–632. https://doi.org/10.1016/j.cep.2006.01.007

Wu, J., Pullum, L., 2000. Performance analysis of axial-flow mixing impellers. AIChE J. 46, 489–498. https://doi.org/10.1002/aic.690460307

Wyrobnik, T.A., Ducci, A., Micheletti, M., 2020. Advances in human mesenchymal stromal cell-based therapies – Towards an integrated biological and engineering approach. Stem Cell Res. 47, 101888. https://doi.org/10.1016/j.scr.2020.101888

Yamamoto, K., Sokabe, T., Watabe, T., Miyazono, K., Yamashita, J.K., Obi, S., Ohura, N., Matsushita, A., Kamiya, A., Ando, J., 2005. Fluid shear stress induces differentiation of Flk-1-positive embryonic stem cells into vascular endothelial cells in vitro. Am. J. Physiol. - Hear. Circ. Physiol. 288. https://doi.org/10.1152/ajpheart.00956.2004

Zhu, H., Nienow, A.W., Bujalski, W., Simmons, M.J.H., 2009. Mixing studies in a model aerated bioreactor equipped with an up- or a down-pumping "Elephant Ear" agitator: Power, hold-up and aerated flow field measurements. Chem. Eng. Res. Des. 87, 307–317. https://doi.org/10.1016/j.cherd.2008.08.013